

Minerva Access is the Institutional Repository of The University of Melbourne

Author/s:

Meng, J;Cadusch, JJ;Crozier, KB

Title:

Plasmonic Mid-Infrared Filter Array-Detector Array Chemical Classifier Based on Machine Learning

Date:

2021-02-17

Citation:

Meng, J., Cadusch, J. J. & Crozier, K. B. (2021). Plasmonic Mid-Infrared Filter Array-Detector Array Chemical Classifier Based on Machine Learning. *ACS Photonics*, 8 (2), pp.648-657. <https://doi.org/10.1021/acsp Photonics.0c01786>.

Persistent Link:

<https://hdl.handle.net/11343/294857>

Plasmonic mid-infrared filter array-detector array chemical classifier based on machine learning

Jiajun Meng^{†}, Jasper J. Cadusch[†], and Kenneth B. Crozier^{*†‡§}*

[†] Department of Electrical and Electronic Engineering, The University of Melbourne, Victoria 3010, Australia.

[‡] School of Physics, The University of Melbourne, Victoria 3010, Australia.

[§]-Australian Research Council (ARC) Centre of Excellence for Transformative Meta-Optical Systems (TMOS), University of Melbourne, Victoria 3010, Australia.

ABSTRACT

Numerous applications exist for chemical detection, ranging from the industrial production of chemicals to pharmaceutical manufacturing, environmental monitoring and hazardous risk control. For many applications, infrared absorption spectroscopy is the favored technique, due to attributes that include short response time, high specificity, minimal drift, in-situ operation, negligible sample disruption, and reliability. The workhorse instrument for infrared absorption is the Fourier transform infrared (FTIR) spectrometer. While such systems are suitable for many purposes, new applications would be enabled by small, lightweight, low power and low cost infrared microspectrometers. Here we perform a detailed study on a microspectrometer chemical classifier comprising an array of plasmonic mid-infrared spectral filters used with a photodetector array, whose outputs are analyzed by a machine learning algorithm. We conduct

simulations (including noise), demonstrating the identification of six gas-phase and six liquid-phase chemicals. We study the performance of our method at detecting the concentration of acetylene.

KEYWORDS: long-wave infrared, microspectrometers, chemical detection, spectroscopy, absorption spectrum

INTRODUCTION

Many applications exist for the identification of materials via their mid-infrared (MIR) fingerprints. Examples include biosensing, the detection of hazardous chemicals in industrial plants and environmental monitoring. At the time of writing, the traditional platform for MIR spectroscopy is the Fourier transform infrared (FTIR) spectrometer. Such systems achieve high resolution and are suitable for many purposes. However, applications exist for which the size, weight and cost of conventional FTIR spectrometers are prohibitive and for which only modest resolution is needed. This motivates the development of miniaturized infrared microspectrometers. Much of previous work on miniaturized microspectrometers has concerned the visible to near-infrared wavelength range, with integrated systems that use complementary metal oxide semiconductor (CMOS) and related technologies having been demonstrated.(1, 2, 3, 4, 5) For the MIR, a variety of microspectrometer approaches that have been explored. IR microspectrometers based on micro-electro-mechanical systems (MEMS) have included voltage-tunable Fabry-Pérot (FP) filters,(6, 7, 8) scanning mirrors,(9) and tunable metamaterials.(10) While these have been shown to be effective, sophisticated multi-step fabrication processes are needed. MIR spectrometers based on silicon photonics have included those employing III-V integration (11) and other approaches such as suspended micro-ring resonators.(12) While impressive results have been obtained, these works also require advanced fabrication methods.(11, 12) In addition, for Ref[(12)], spectrometer read-out requires a tunable laser. MIR spectrometers based on what is sometimes termed the filter array – detector array (FADA) configuration have been shown.(13, 14, 15, 16, 17, 18, 19, 20) In a FADA microspectrometer, an array of spectral filters is integrated with an array of detectors.(3, 13, 14,

15, 16, 17, 18, 19, 20, 21, 22, 23, 24) Compared to the aforementioned approaches to MIR spectrometers, the FADA method offers several benefits. First, at the time of writing, infrared detector arrays have become available at low cost, being developed for thermal imaging applications for the consumer market. One may therefore realize a FADA microspectrometer by adding a filter array to such a detector array. Second, the fabrication process needed for a FADA device is relatively simple. Third, FADA spectrometers have no moving parts. They are therefore robust and do not require the dedicated electronic driving circuits needed for electrostatic actuators. For these reasons, in this paper we consider MIR microspectrometers based on the FADA approach. Linear variable filters (LVF(13, 14, 15, 16)) and plasmonic (18, 19, 20) filters have been used in studies of MIR FADA microspectrometers. Here, we study a FADA system based on plasmonic filters. This is motivated by the fact that they can be made relatively easily by the lift-off process and can span a wide operating range from the visible to the mid-IR.(18, 25, 26, 27, 28, 29, 30, 31, 32, 33) We note nonetheless that our approach could also be used with FADA microspectrometers based on LVF devices.

A traditional approach to chemical detection/identification consists of measuring the infrared absorption spectrum (of the material under question) and matching it with a database containing the spectra of different chemicals. While this approach generally works well for most purposes, for applications for which the use of a high-resolution spectrometer is infeasible, other methods can be considered. Here we use machine learning (ML) to directly analyze the microspectrometer outputs and determine the chemical species (and/or concentration), without the intermediate step of finding the infrared absorption spectrum. ML enables the exploitation of latent data structures and facilitates the classification of highly nonlinear data, and there has thus been much interest recently on its use for photonics.(34) ML algorithms have been used for super-resolution imaging,(35, 36) for the inverse design of metasurfaces by predicting optical spectra,(37, 38, 39) for metasurface microwave imaging(40, 41) and in a gas-sensing electronic nose.(42, 43) ML algorithms have also been used for computational spectroscopy at visible wavelengths(3, 4, 5, 22) and in the infrared.(18, 19, 20, 44) To the best of our knowledge, this work

represents the first time that ML has been investigated for chemical identification/quantification with infrared microspectrometers.

Here, we present a thorough numerical study on chemical detection and quantification with an infrared microspectrometer consisting of plasmonic metasurface spectral filters used with an array of detectors. We term this configuration a filter-array detector-array (FADA) spectrometer. The filters are band-stop and band-pass designs that cover the mid-infrared (IR) band. Infrared metasurfaces have been shown to present exciting opportunities for molecular and bio-sensing.(45, 46, 47, 48, 49) In those works, the biomolecules were adsorbed onto the metasurfaces. By contrast, in our method, the chemicals to be detected/quantified do not need to adsorb onto the metasurface, meaning that the latter can be re-used. Our work is motivated in part by the recent emergence of small, lightweight (<1 g), low-cost and low-power MIR thermal imaging cameras. These devices could be used as the detector in our proposed FADA spectrometer. To investigate this approach, the responsivity spectrum of the detector array used in our numerical model is chosen to be that of a specific uncooled thermal camera which is available on the consumer electronics market at the time of writing. We conduct simulations that demonstrate material identification by readout of the detector array using support vector machine (SVM) classifiers. We study the performance of our approach in determining the concentration (to nearest order of magnitude) of acetylene gas down to 10 ppm. We discuss the selection of the most suitable ML algorithm, the training of ML classifiers and our approach for performance evaluation of the trained ML models. We conclude this paper with a summary of key findings and a brief discussion of future work.

NUMERICAL MODEL

In this work we model the use of a filter array detector array (FADA) microspectrometer to identify and quantify (i.e. determine concentration range) of a variety of gas- and liquid-phase chemicals based on their IR absorption spectra. The FADA microspectrometer is schematically depicted in Figure 1a. This platform integrates a plasmonic filter array with a detector array. Light from an infrared light source

illuminates the analyte, i.e. the chemical to be detected, with the transmitted light illuminating the device. The spectrum of light impinging upon each detector pixel is thus the product of the source spectrum, the analyte transmission spectrum and the transmission spectrum of the corresponding element of the plasmonic filter array. We simulate the collection of training data in which different chemicals at a variety of concentrations are present and the detector outputs are sampled. We then simulate the identification/quantification of various chemicals, using this training data and a ML classification model. Our numerical model includes noise, with the assumed signal to noise ratio (SNR) ranging from 10 to 200. As discussed, to make the model as representative as possible of how it could be implemented in practice, we take the responsivity spectrum of the detector array to be that of a specific uncooled thermal camera that is available on the consumer market at the time of writing, the FLIR Lepton (FLIR Systems, Inc.). This uses a microbolometer array and has responsivity over the wavelength range 6 to 14 μm . We choose to model a system with a relatively modest number of filters (40), which would be readily achievable with the FLIR Lepton which has 4800 (80 \times 60) pixels.

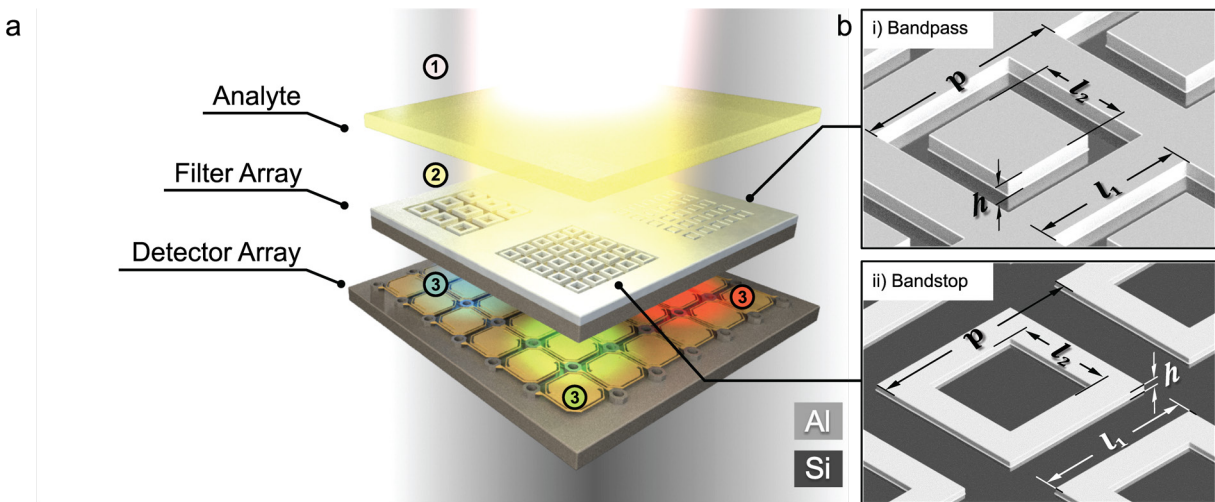


Figure 1. (a) Filter array detector array (FADA) system schematic. (1) Light from IR source (not shown) is filtered by analyte (liquid/gas chemical to be identified or quantified) placed in optical path. (2) Transmitted light is filtered by plasmonic filter array which contains bandpass and bandstop mid-IR filters. (3) Detectors convert optical power into electrical signals. **(b)** Schematic illustration of unit cell structure of **(i)** Bandpass filter and **(ii)** bandstop filter.

We next describe our plasmonic filter array. Undoped silicon is chosen as the substrate for the plasmonic filter arrays because it has high transmittance in the wavelength range of interest (6 to 14 μm) and is

readily available at low cost. Aluminum is chosen as the plasmonic material, due to its low cost, CMOS fabrication process compatibility and chemical inertness, a consequence of its self-passivated surface. The filters may be divided into two categories: bandpass filters (square arrays of rectangular coaxial apertures in the aluminum film) and bandstop filters (square arrays of rectangular aluminum rings). Unit cells of the two filter types are shown in Figure 1b. The geometric parameters p, h, l_1, l_2 (Figure 1b) determine the resonances of these structures. The period p strongly influences the center wavelengths of the passbands and stopbands of the transmittance spectra, with the other parameters modifying the widths of these bands. By appropriate choice of these parameters, therefore, the bandpass and bandstop features can be tuned across the wavelength range over which the detector we model (FLIR Lepton) is responsive ($\lambda = 6$ to $14 \mu\text{m}$). Finite difference time domain (FDTD) simulations of the filters are presented as Figure 2a. The complex refractive indices of Si and Al are taken from references [(50, 51)]. It can be seen that both the bandstop and bandpass filters have relatively broad full width at half maximum (FWHM) values. Within each filter class, the correlations between filters are higher than desired. This motivates our use of two filter types as this reduces the correlations. An analysis of filter correlations can be found in the Supporting Information (see Figure S1). In Figure 2a, the transmission spectra are plotted against array period p . The other geometric parameters of the filters are as given in Table 1. The transmission bandstop (notch) and bandpass features both shift to longer wavelengths with array period. The fabrication of the plasmonic filter array could be realized using standard microfabrication processes, i.e. lithography, physical vapor deposition (PVD) and liftoff. Two PVD steps would be needed, as the bandpass and bandstop filters use different Al thickness. A discussion on the choice of the thickness of the aluminum layer is included in Supporting Information (see Figure S2). A process that could be used to fabricate the device is shown as Figure S3. From Figure 2a, it can be seen that the FWHMs of the bandpass filters range from 2.3 to $3.9 \mu\text{m}$. For the bandstop filters, the FWHMs range from 1.8 to $2.5 \mu\text{m}$. The peak transmission of the bandpass filters ranges from 0.545 to 0.565 . The minimum transmission of the bandstop (notch) filters is as low as 0.004 over the wavelength range considered (6 - $14 \mu\text{m}$). In Figure 2b, we plot the product of the filter transmission spectra with the responsivity spectrum of the thermal image

sensor assumed in this work (FLIR Lepton). The responsivity spectrum is from the manufacturer’s datasheet and is also provided as Figure S4.

Table 1. Filter Geometric Parameters

	l_1	l_2	h
Bandpass	$0.6p$	$0.4p$	140 nm
Bandstop	$0.5p$	$0.3p$	50 nm

We next describe how the chemical analytes are modelled. This is both for the simulations that model the ML training step as well as those that test the chemical detection/quantification capabilities. We use 12 analyte spectra, calculated using the absorption cross section spectra provided in References [(52, 53, 54, 55)]. To simplify the notation, we introduce the term normalized molarity, defined as the molarity (molar concentration) divided by the molarity of the analyte when in pure form, expressed as a percentage. For example, the molarity of pure chloroform (measured at one atmosphere and at a temperature of 298 K) is 12.5 M. If a diluted chloroform sample has a molarity of 1.25 M, then its normalized molarity is 10%. The transmission spectra of the analytes we consider at normalized molarities of 10% and 100% are shown as Figure 2c. For the liquids considered, the path length is taken as 0.01 cm. For the gases, the path length is taken to be 10 cm. These path lengths are chosen based on values typical in liquid/gas cells. Diluents that would be suitable for experimental measurements include nitrogen (for the gases) and CS₂ (for the liquids). These have negligible absorption in the wavelength range we consider. We assume that experiments would be conducted at room temperature (298 K). For the gas experiments, atmospheric pressure (1 atm) is assumed. The IR light source is taken as blackbody radiation at 373.15K, with the spectrum shown as Figure S5.

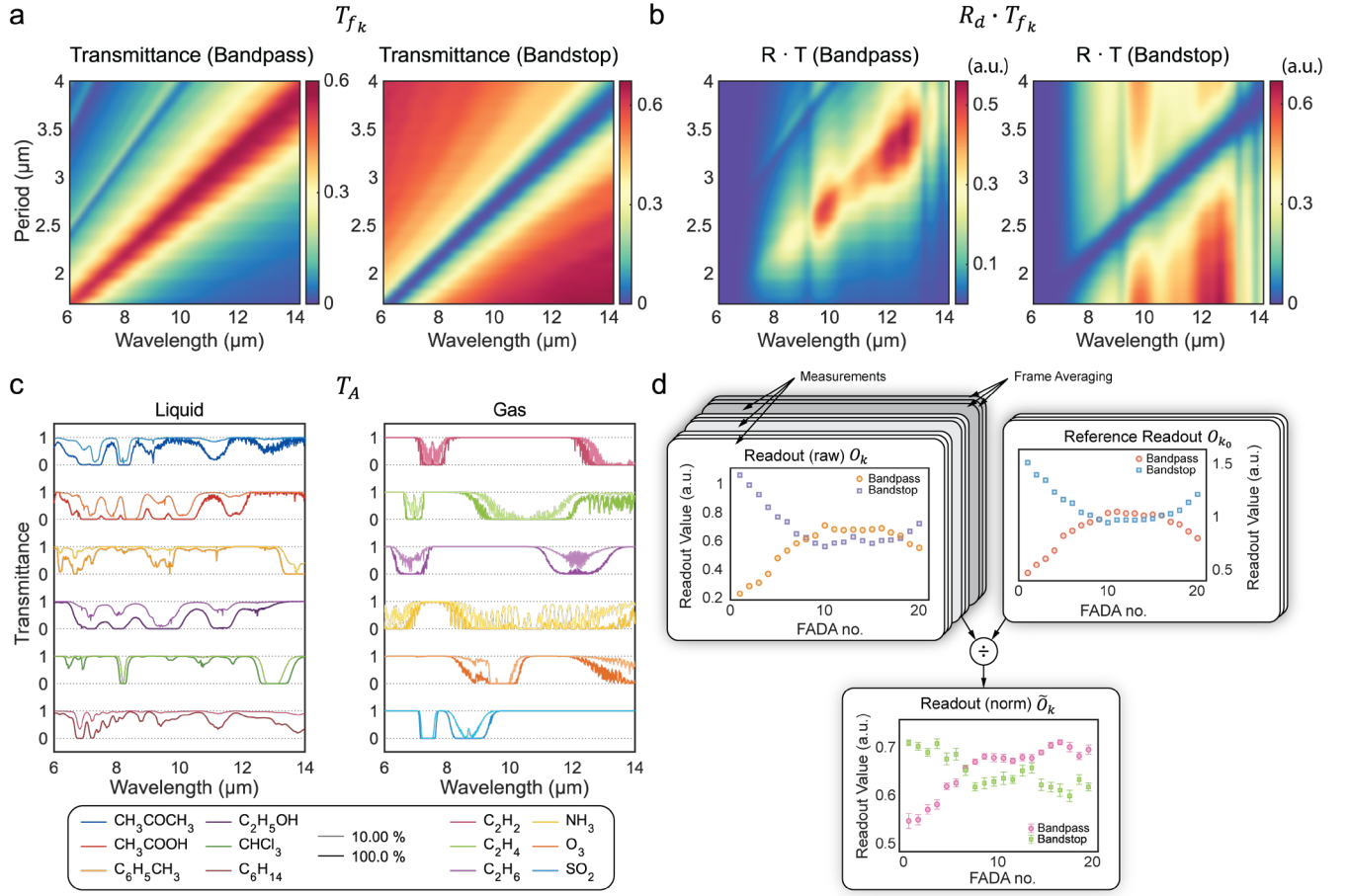


Figure 2. Generation of machine learning training data. **(a)** Simulated transmittance spectra T_{fk} of bandpass and bandstop filters. **(b)** Product of simulated transmission spectra (T_{fk}) with detector responsivity (R_d), i.e. $R_d T_{fk}$. Filters used in FADA spectrometer model have periods ranging from 2.08 to 3.60 μm , in steps of 80 nm. **(c)** Transmittance spectra T_A of 12 selected liquid and gas analytes with normalized molarities of 10% (lighter curves) and 100% (darker curves). **(d)** Schematic illustration of conversion from raw noisy readout data O_k to machine learning training data \tilde{O}_k . Error bar plot of normalized FADA readout \tilde{O}_k . This example is based on mean and standard deviation of twenty simulated measurements of neat acetone.

We next describe the model used to determine the FADA readout, i.e. detector signals that would be recorded by the system. The raw output of each FADA channel can be modeled as follows,

$$O_k = n_k + \int_{\lambda_1}^{\lambda_2} I_s \cdot T_A \cdot R_d \cdot T_{fk} d\lambda \quad (1)$$

where I_s is the power spectrum of the infrared light source, T_A is the analyte transmittance, R_d is the responsivity of the detector, and O_k, n_k, T_{fk} are the raw readout, total noise and transmittance of the k^{th} filter element, respectively. R_d is taken from the Lepton datasheet specification (56) and is shown as

Figure S4. The product of R_d and T_{f_k} , i.e. the combined responsivity of the k^{th} plasmonic filter and the k^{th} detector of the array, is shown in Figure 2b. As aforementioned, the total number of FADA elements is 40. We choose this to consist of 20 bandpass and 20 bandstop filters. The transmittance spectra of the 40 filters are as shown in Figure S6. To mitigate against the deleterious effects of changes in the source spectrum and in the camera responsivity spectrum that could occur in practice (i.e. in experiments), it would be advantageous for the raw readout to be normalized using a reference output. We do so here, to model what one would do in practice as closely as possible. The reference output is recorded when there is no analyte present in the optical path length (i.e. void):

$$O_{k_0} = n_{k_0} + \int_{\lambda_1}^{\lambda_2} I_s \cdot R_d \cdot T_{f_k} d\lambda, \quad k = 1, 2, 3, \dots, 40 \quad (2)$$

where n_{k_0} is the total noise when recording the reference readout frame.

The normalized readout \tilde{O}_k is defined as:

$$\tilde{O}_k = \frac{O_k}{O_{k_0}} \quad (3)$$

To ensure that our model is realistic, we include noise that is assumed to be Gaussian. To understand how system performance varies with noise, we vary the latter so that the signal-to-noise ratio (SNR) ranges from 10 to 200. We investigate how system performance varies with the use of averaging of multiple data sets. This is referred to as ‘‘frame averaging’’ (FA). The normalized value \tilde{O}_k of each frame-averaged data set is given by the following expression,

$$\tilde{O}_k = \frac{\langle O_k \rangle}{\langle O_{k_0} \rangle}, k = 1, 2, 3, \dots, 40 \quad (4)$$

where $\langle O_k \rangle, \langle O_{k_0} \rangle$ are the frame averaged versions of the O_k, O_{k_0} . This process is schematically illustrated in Figure 2d.

The numerical model described above is used to generate data for training ML classifiers. Since the same kind of analyte at different molarities produces different readout \tilde{O}_k patterns, we construct the library of spectra so that it contains all twelve analytes at different molarities. This is motivated by our

desire to improve identification accuracy. These include normalized molarities varied in steps of one order of magnitude, e.g. 1, 0.1, 0.01. These spectra are calculated from the absorption cross section spectra using the Beer-Lambert law. In Figure 3a, we show such spectra for the examples of CHCl_3 and SO_2 . From the spectra, we use equation 4 to calculate the corresponding normalized readout library for the SNR value that is assumed. The process is stochastic. The process thus needs to be repeated multiple times so that the results are statistically meaningful. To do so, we generate 20 readouts of a single analyte at a specific normalized molarity level. This is illustrated in Figure 3b-c where FADA readouts of two analytes at three molarity levels are presented in error bar plots. Note that ten frames are averaged for each readout. The reduction in size of the error bars after frame averaging (FA) clearly indicates the benefits of the latter. At this point, however, in our library of spectra the normalized molarities vary in large increments. To address this, we use interpolation to estimate spectra at intermediate molarity values. Our method is validated by a simulated identification accuracy test. We discuss this in detail later in the paper.

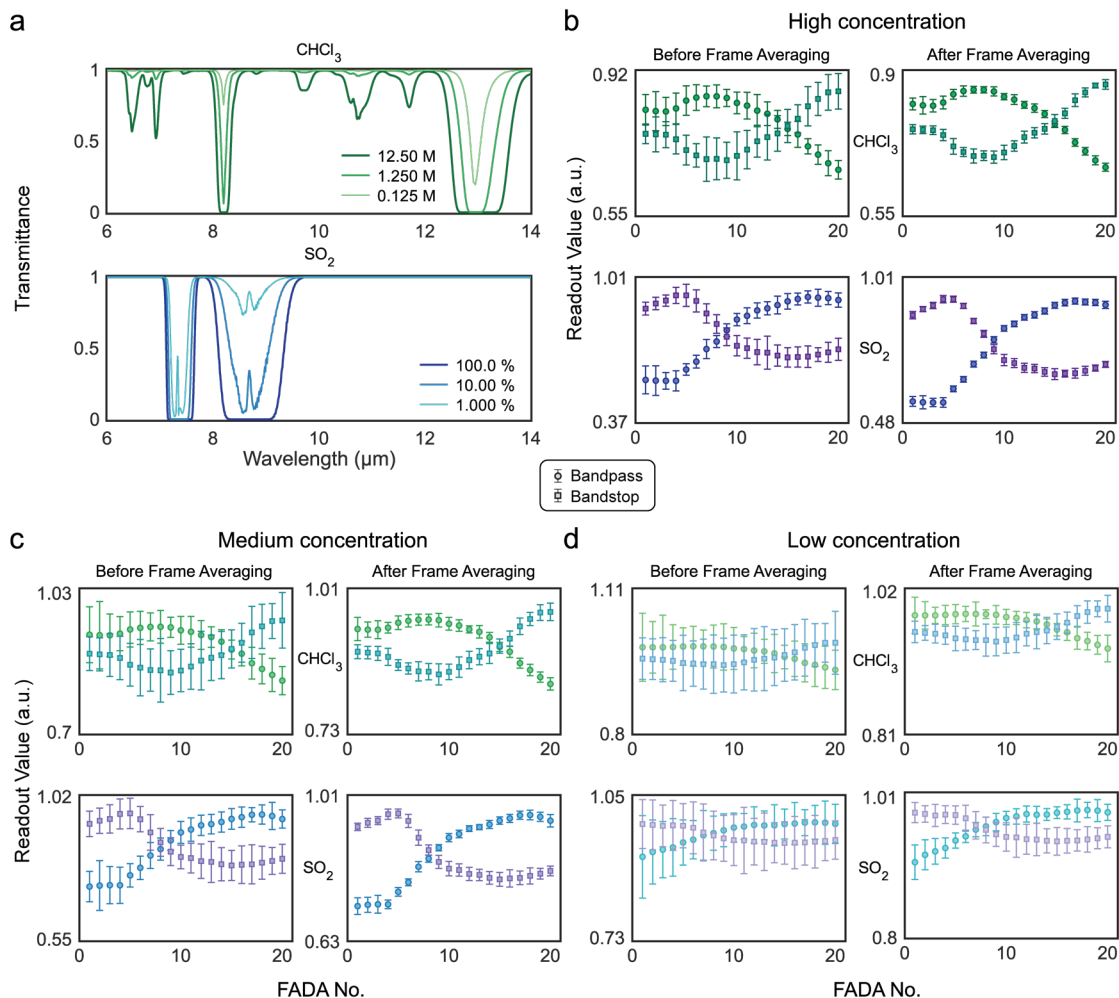


Figure 3. Example of training data using different analytes with different molar concentrations under influence of noise. **(a)** Transmittance spectra of CHCl_3 and SO_2 at three different normalized molarity levels of 100%, 10% and 1%. **(b)-(d)** Normalized readout of FADA device for two chemicals (CHCl_3 and SO_2) at three molarity levels before and after frame averaging (FA, ten frames). Model includes noise, with signal to noise ratio (SNR) assumed to be 20. Error bar plots represent mean and standard deviation of readout values. FA significantly reduces the readout variance.

We plan to experimentally demonstrate this concept based on this model in the future. We anticipate that our interpolation method will also be beneficial for the experimental realization of this concept, reducing the number of analyte concentrations at which the system must be characterized. We hereafter use the term “fully simulated readout” to refer those generated using Eqns (1-4) as described above. We use “interpolated readout” to refer to the data sets produced by interpolation. The fully simulated and interpolated readouts are combined to form the training data for ML classifiers. The step-by-step process for training preparation and an example of a training data table are schematically illustrated as Figure S7.

MACHINE LEARNING CHEMICAL IDENTIFICATION

In this section, we describe our machine learning (ML) approach and results. The FADA microspectrometer concept we investigate generates a collection of observations (readout data), with our goal being to identify to which analyte each observation belongs. This is a classification problem and can be solved using a variety of machine learning algorithms, such as k-nearest neighbors,(57) decision tree,(58) discriminant analysis classifier,(59) neural network classifier,(60) and support vector machines.(61) We investigate the aforementioned algorithms and find that support vector machines (SVMs) provide the highest accuracy for the chemical identification problem (see Table S1). We therefore use it in the remainder of this study. During the training of its classifier, an SVM model takes points in multidimensional space and outputs the hyperplanes that best separate the point clusters. When given new (i.e. non-training) data, the SVM classifies it by comparing its location in multidimensional space with the hyperplanes (found in the training step). The SVM method is commonly used for binary classification applications. However, the chemical identification task we consider is a multiclass classification problem. We therefore transform it into a set of binary classification problems so that the SVM method can be applied.(62) In such a multiclass classification scenario, the SVM method is usually combined with an error correcting output code (ECOC) algorithm to improve accuracy.(63) In this work, we do so.

We feed the collected readout data to the SVM algorithm to train a classification model that identifies which chemical is present. We also train a classification model that determines the concentration of a specific analyte. To illustrate the method, in Figure 4a, we provide an example in which this approach is used to classify the simulated measured analyte into one of six classes. These comprise five different chemicals (acetone, ethanol, acetic acid, toluene, and chloroform) and the case where no chemical is present. We hereafter use “void” to refer to the latter. Each analyte is sampled five times at each molarity level (0.001, 0.1 and 1). Note that details on how data preparation is performed for the results shown as Figure 3 and Figure 4 are included in the Supporting Information. Note that we limit the number

of concentration levels in this example to make the results easier to interpret. We assume that the signal to noise ratio (SNR) of each simulated measured frame is 10, which should be readily achievable. We assume that 81 frames are used in the frame averaging (FA) process, which would comprise three seconds of data at the frame rate (27 fps) at which the sensor assumed in this work (FLIR Lepton) operates. Principal component analysis (PCA) is applied to reduce data dimensionality from the 40 dimensions of the raw data that arise from the 40 outputs. This enables us to plot the data in a lower dimensional space in Figure 4a by maximizing the variance of each dimension.⁽⁶⁴⁾ The PCA analysis shows that, for this example, most of the data variance is in the first two (99.2% explained variance) or first three (99.6% explained variance) principal components (PCs). We can thus visualize the data in two (Figure 4a(i)) or three (Figure 4a(ii)) dimensional space. K-fold cross validation is often used to evaluate the performance or to estimate the skill of machine learning classification models on unseen data.⁽⁶⁵⁾ The parameter K refers to the number of groups that the (shuffled) training data is split into. One group at a time is held out for testing using a classifier trained by the remaining (K-1) groups. This process is repeated for K times to calculate the overall accuracy which is defined as the quotient of the number of correct classifications to the number of training data sets. Here we train two 10-fold cross validated classifiers using the first two or three PCs and evaluate the results. The SVM kernel for this model is cubic polynomial. In Figure 4a, each cluster consists of five data points and corresponds to a certain analyte at a certain concentration. The trajectory followed by the clusters as concentration is reduced leads to the ‘void’ class, which is to be expected as this represents a concentration of zero. The spatial extent of each cluster in the 2D representation of Figure 4a indicates the impact of noise. In Figure 4a(i), we use color to denote to which analyte each location in 2D PCA-space would be classified to. The boundaries of adjacent colored shadings in Figure 4a(i) thus represent decision boundaries. Similarly, the SVM hyperplanes are shown as colored surfaces in Figure 4a(ii). It can be seen that at the higher concentration levels, the classifier trained with two PCs works well, with the different chemicals correctly identified and the clusters being well contained in the appropriate regions. At the lowest concentration considered, the clusters are usually in the correct regions i.e. the chemicals are correctly identified. Sometimes however they are not, i.e. the

chemical is misidentified as being another chemical or as being void (no chemical present). The 10-fold cross validation accuracy of this classifier is 95.45%. That this is not 100% is due to the fact that, when the analyte concentration is low, the clusters are located closer to the ‘void’ class and some data points are in the void region, meaning that the analyte is misidentified. For the classifier trained with three PCs, the cross-validation prediction accuracy increases to 98.18%. While the explained variance of this additional PC is very small (PC1 & PC2 99.2%, PC3 0.4%), it is essential for the model to correctly classify analytes at low concentrations. In other words, PC3 provides information that allows the classifier to more precisely find the hyperplane that can separate the analyte clusters from the ‘void’ clusters.

We next explore a more complicated scenario in which we include seven classes and 20 simulated measurements per condition. We train one classifier for the liquid analyte group and another for the gas analyte group. We adopt the same values for the SNR (10) and FA conditions (81 frames) as before. We find both classifiers have cross-validation accuracies greater than 95%. For the liquid analyte classifier, we consider six chemicals (chloroform, acetone, acetic acid, ethanol, hexane, and toluene) and the “void” class (i.e. no chemical present). For the gas classifier, we consider six chemicals (C_2H_2 , C_2H_4 , C_2H_6 , NH_3 , O_3 , and SO_2) and the “void” class. We try different kernel functions for SVM. We find that the Gaussian SVM kernel function has the greatest accuracy for the liquid analytes while the cubic polynomial kernel function has the greatest accuracy for the gas analytes. We thus employ these techniques.

To quantify the performance of our approach, we present the results in the form of confusion matrices as Figure 4b and Figure 4c. The 10-fold cross-validation accuracy values are 98.69% and 95.34% for liquid and gas analytes, respectively. The true positive (TP) and false negative (FN) rates of each analyte are listed on the right of the confusion matrix. The fact that the gases are identified with lower accuracy on average than the liquid is largely due to the results for ethane. The absorption cross section for ethane in the wavelength range considered is smaller than for the other gases, making it more difficult for the classifier to distinguish it from void when in low molarity. Information on how the performance of this approach varies with SNR and FA is provided in the Supporting Information (see Figure S8). At high SNR and FA, high performance can be achieved.

It might be helpful for some applications to know whether or not certain gases (or liquids) are present, for the case that the possible gas (or liquid) concentration spans a wide range. We therefore test our model in this scenario. We generate 1000 data points for the gases, with the gas species (i.e. C_2H_2 , C_2H_4 , C_2H_6 , NH_3 , O_3 , or SO_2) and normalized molarity (between 0.001 and 1) being chosen randomly. We also generate 1000 data points for the liquids, with the species (i.e. chloroform, acetone, acetic acid, ethanol, hexane or toluene) and normalized molarity (between 0.01 and 1) again chosen randomly. We assume that the SNR and FA number are the same as those used in the training (i.e. 10 and 81, respectively). We use our classification model trained with the entire training data to estimate the gas species for each data point. This is also done for the liquid data points. For gas identification, the model identifies the gas correctly 942 times (out of 1000). For liquid identification, correct identification occurs 980 times (out of 1000). As one might expect, the misclassified data points are usually those corresponding to analytes at low concentrations.

The high accuracy of the model confirmed by these results confirms the efficacy of the interpolation process we use for preparing the training data. As discussed, we generate data for analytes at a few different molarities using Eqns (1-4) and use interpolation to predict the results at other molarities. The trained classifier model is nonetheless shown to be able to identify analytes with any concentration in the detection range.

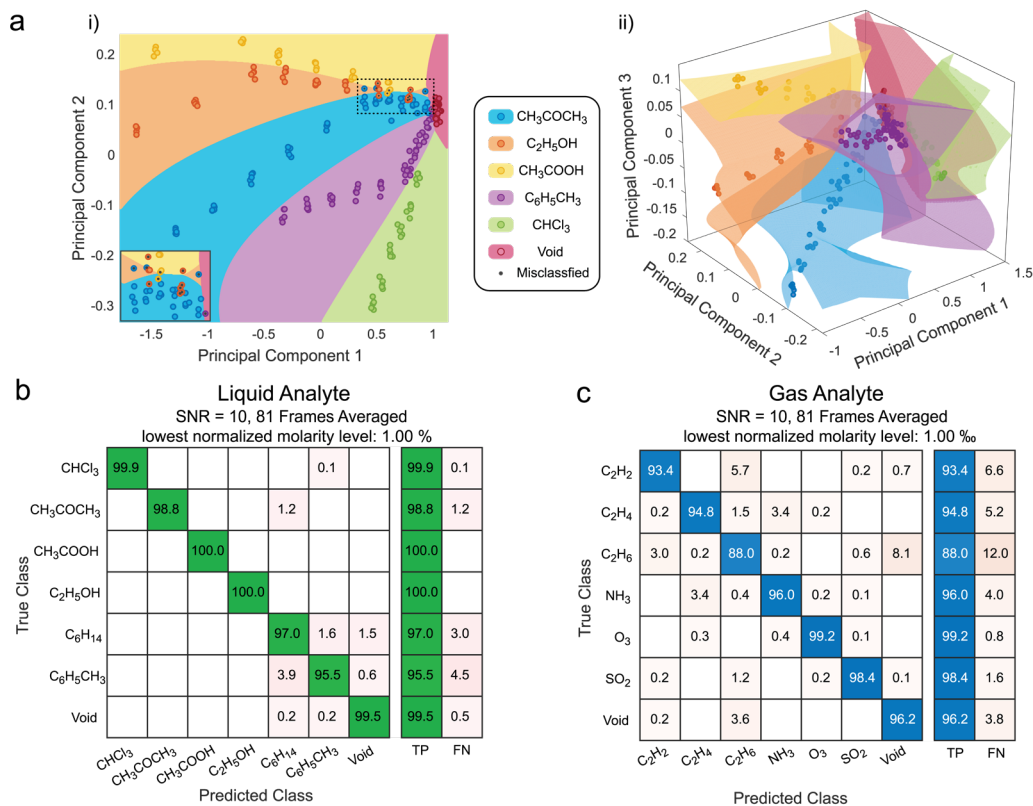


Figure 4. Classification results. **(a)** Visualization of classification results for five analytes, with SNR of 10 and an 81-frame averaging process. Data projected into **(i)** space of first two principal component (99.2% explained variance) and **(ii)** space of first three principal components (99.6 % explained variance). Colored regions in panel **(i)** represent class into which chemical is classified. Colored planes in panel **(ii)** denote hyperplanes separating different analytes. Inset shows zoom-in of low concentration/void region, with misclassified data points indicated by additional black dot. **(b)** Confusion matrix for liquid analyte classification results. **(c)** Confusion matrix for gas analyte classification results.

We next show that our proposed system can determine the concentration level of a known analyte. By “concentration level”, we mean the concentration to within one order of magnitude. We train the SVM classifier by assigning the correct concentration level to each data point. Here we demonstrate the concentration level detection of acetylene (C₂H₂) for different choices of SNR and FA number. Six class labels are assigned, comprising 10¹ to 10² ppm, 10² to 10³ ppm, 10³ to 10⁴ ppm, 10⁴ to 10⁵ ppm, 10⁵ to 10⁶ ppm and ‘void’. Classification model confusion matrices obtained for four different SNR and FA number combinations are presented in Figure 5a. The cross-validation classification accuracy values are 88.28%, 91.31%, 99.4% and 99.46%. Results for another two combinations of SNR (=50) and FA number (=135 and 270) are provided in Supporting Information (see Figure S9). To help visualize the results, the results for SNR=20 and FA=135 (i.e. ~5 s of data) are shown as Figure.5b. From the inset, it can be seen that at

the lowest two concentration bands (10^1 to 10^2 ppm and 10^2 to 10^3 ppm), the data point clusters merge together with those of the “void”, meaning that the classifier decreases in accuracy. We next consider what accuracy might be achievable if the SNR and FA were to be improved. To do so, we train a large set of classification models under different combinations of SNR and FA and determine the validation accuracy in each case. A surface plot of the classification accuracy as a function of SNR and number of frames (FA number) is shown as Figure 5c. The four conditions considered in Figure 5a are indicated on the plot (Figure 5c) by color-coded circles. It can be seen that the accuracy quickly converges to what might be regarded as a fairly high value (of $\sim 95\%$) as the SNR and/or FA number are increased. Further increases in SNR and/or FA number result in only minor improvements in accuracy once this “plateau” is reached. This plot could be used to determine the appropriate tradeoff between the time interval between results (due to FA) and the accuracy. In other words, when the system SNR is known, one may use the plot to determine the minimum FA needed to achieve a certain validation accuracy, e.g. 95%. We also conduct simulations using fewer filter elements and evaluate the impact on the performance. A discussion on this is included in Supporting Information (See Figure S10). We run a similar simulated test on classification (iv), i.e. SNR=200 and FA=270. We generate 1000 data points at different concentrations including ‘void’. We find a classification accuracy greater than 99%. As one might expect, many of the classification errors are near the boundaries of the concentration levels, e.g. 1.2×10^2 ppm belongs to the range 10^2 to 10^3 ppm, but might be misclassified as being in the 10^1 to 10^2 ppm class. We note that in experiments, a number of factors (e.g. atmospheric composition, humidity, temperature, et.c.) could influence the sensor performance. The results we present should thus be taken as an estimate (rather than a precise determination) of performance.

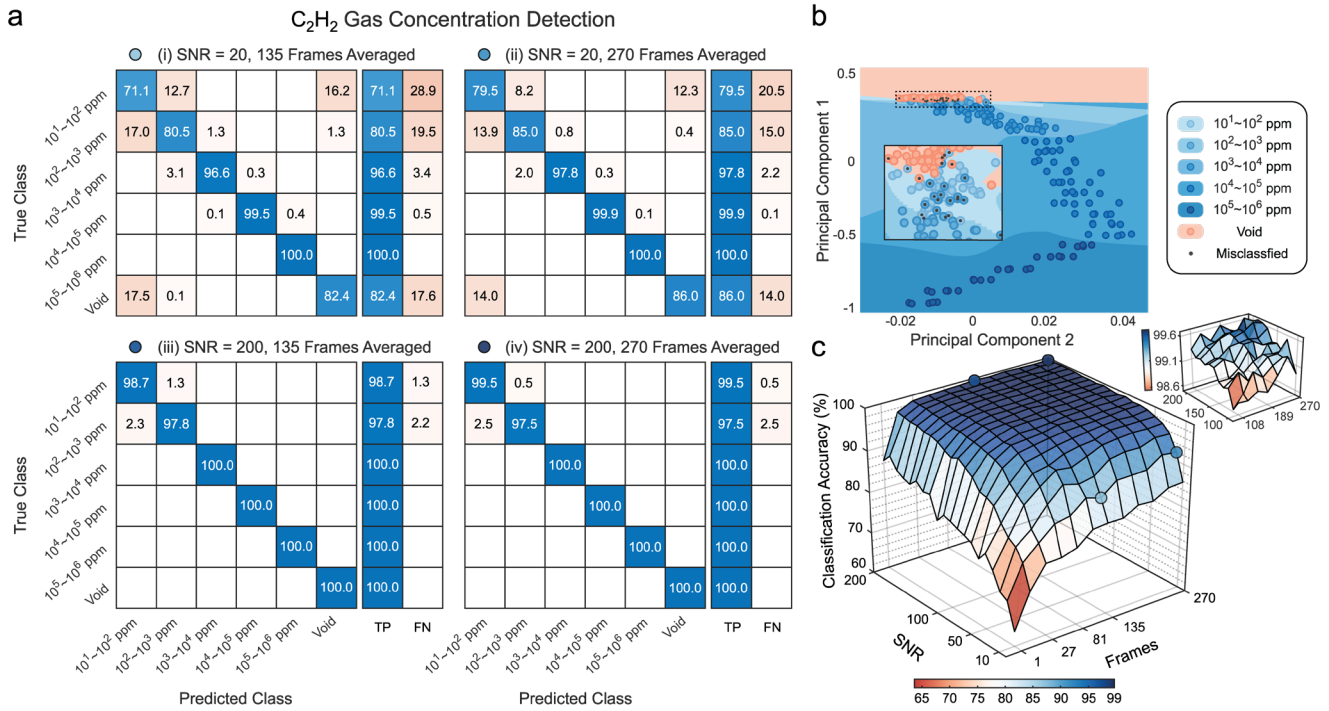


Figure 5. Gas concentration detection results. **(a)** Confusion matrices of acetylene concentration detection under different noise and FA condition **(i)-(iv)**. Model considers concentrations down to 10 ppm. **(b)** Visualization of classification results of gas concentration detection. Simulated readout data points are projected into the space of first two principal components (99.68% explained variance). Inset shows the simulated readout data is misclassified at the lowest concentrations. **(c)** Surface plot of classification accuracy as the function of SNR and number of frames. Inset shows the ‘plateau’ area of the main plot.

CONCLUSION

In this work, we study the concept of using a filter array detector array (FADA) microspectrometer and a machine learning classification algorithm to realize material identification and concentration detection. We simulate and design an array of aluminum plasmonic filters on a silicon substrate. The filter spectral features cover the 6-14 μm MIR range. We model the FADA by combining the simulated transmission spectra of the plasmonic filters with the responsivity spectrum of a thermal imaging camera that is available at low cost at the time of writing. We use the simulated readout of the detector array including noise for training classification models. Our result predict that the proposed system would identify analytes from a group of chemicals with high accuracy. Furthermore, we show that the same system can also be deployed to detect the order of magnitude of concentration of a specific gas analyte. Future work could focus on the optimization of filter design and the experimental demonstration of this method.

ASSOCIATED CONTENT

Supporting Information

The Supporting Information is available free of charge on the ACS Publications website.

Discussion of the correlations of filter transmittance spectra and choice of filter types. Discussion of thickness of the aluminum layer. Source Spectrum and detector responsivity used for numerical model. Transmittance and responsivity of the selected 40 filters and FADA elements. Training data preparation and one observation example for machine learning classification model training. Relationship between the classifier performance and noise conditions and number filter elements

AUTHOR INFORMATION

Corresponding Authors

Jiajun Meng – Department of Electrical and Electronic Engineering, The University of Melbourne,

Victoria 3010, Australia; <https://orcid.org/0000-0002-8883-1778>; Email:

jiajunm@student.unimelb.edu.au

Kenneth B. Crozier - Department of Electrical and Electronic Engineering, The University of

Melbourne, Victoria 3010, Australia; School of Physics, The University of Melbourne, Victoria 3010,

Australia; <https://orcid.org/0000-0003-0947-001X>; Email: kenneth.crozier@unimelb.edu.au

Authors

Jasper Cadusch - Department of Electrical and Electronic Engineering, The University of Melbourne,

Victoria 3010, Australia; <https://orcid.org/0000-0002-1353-7005>; Email: cadusch.j@unimelb.edu.au

ACKNOWLEDGEMENT

This work was supported in part by the Australian Research Council Discovery Projects scheme

(DP180104141 and DP210103428).

REFERENCE

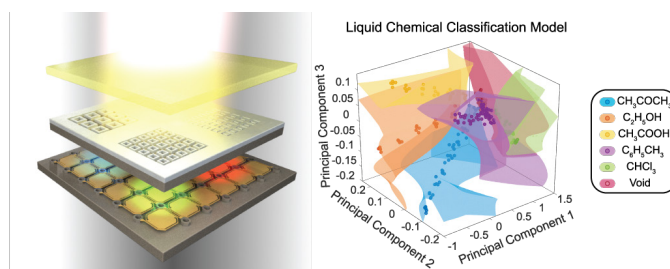
- (1) Correia, J.; De Graaf, G.; Kong, S.; Bartek, M.; Wolffenbuttel, R. Single-chip CMOS optical microspectrometer. *Sens. Actuators, A* **2000**, *82* (1-3), 191-197, DOI: 10.1016/S0924-4247(99)00369-6.
- (2) Wu, H.; Grabarnik, S.; Emadi, A.; de Graaf, G.; Wolffenbuttel, R. F. A thermopile detector array with scaled TE elements for use in an integrated IR microspectrometer. *J. Micromech. Microeng.* **2008**, *18* (6), DOI: 10.1088/0960-1317/18/6/064017.
- (3) Zhu, Y.; Lei, X.; Wang, K. X.; Yu, Z. Compact CMOS spectral sensor for the visible spectrum. *Photonics Res.* **2019**, *7* (9), 961-966, DOI: 10.1364/prj.7.000961.
- (4) Cadusch, J. J.; Meng, J.; Craig, B.; Crozier, K. B. Silicon microspectrometer chip based on nanostructured fishnet photodetectors with tailored responsivities and machine learning. *Optica* **2019**, *6* (9), 1171-1177, DOI: 10.1364/optica.6.001171.
- (5) Meng, J.; Cadusch, J. J.; Crozier, K. B. Detector-Only Spectrometer Based on Structurally Colored Silicon Nanowires and a Reconstruction Algorithm. *Nano Lett.* **2019**, 320-328, DOI: 10.1021/acs.nanolett.9b03862.
- (6) Neumann, N.; Ebermann, M.; Gittler, E.; Meinig, M.; Kurth, S.; Hiller, K. In *Uncooled IR sensors with tunable MEMS Fabry-Pérot filters for the long-wave infrared range*, SENSORS, 2010 IEEE, IEEE: 2010; pp 2383-2387, DOI: 10.1109/ICSENS.2010.5690856.
- (7) Gasser, C.; Genner, A.; Moser, H.; Ofner, J.; Lendl, B. Application of a tunable Fabry-Pérot filter to mid-infrared gas sensing. *Sens. Actuators, B* **2017**, *242*, 9-14, DOI: 10.1016/j.snb.2016.11.016.
- (8) Mao, H.; Tripathi, D. K.; Ren, Y.; Silva, K. D.; Martyniuk, M.; Antoszewski, J.; Bumgarner, J.; Dell, J. M.; Faraone, L. Large-area MEMS tunable Fabry-Pérot filters for multi/hyperspectral infrared imaging. *IEEE J. Sel. Top. Quantum Electron.* **2016**, *23* (2), 45-52, DOI: 10.1109/JSTQE.2016.2643782.
- (9) Zhou, Y.; Wen, Q.; Wen, Z.; Huang, J.; Chang, F. An electromagnetic scanning mirror integrated with blazed grating and angle sensor for a near infrared micro spectrometer. *J. Micromech. Microeng.* **2017**, *27* (12), 125009, DOI: 10.1088/1361-6439/aa85cd.
- (10) Stark, T.; Imboden, M.; Kaya, S.; Mertiri, A.; Chang, J.; Erramilli, S.; Bishop, D. MEMS tunable mid-infrared plasmonic spectrometer. *ACS Photonics* **2015**, *3* (1), 14-19, DOI: 10.1021/acsp Photonics.5b00290.
- (11) Muneeb, M.; Vasiliev, A.; Ruocco, A.; Malik, A.; Chen, H.; Nedeljkovic, M.; Penades, J. S.; Cerutti, L.; Rodriguez, J. B.; Mashanovich, G. Z.; Smit, M. K.; Tourni, E.; Roelkens, G. III-V-on-silicon integrated micro - spectrometer for the 3 μm wavelength range. *Opt. Express* **2016**, *24* (9), 9465-72, DOI: 10.1364/OE.24.009465.
- (12) Vasiliev, A.; Malik, A.; Muneeb, M.; Kuyken, B.; Baets, R.; Roelkens, G. On-Chip Mid-Infrared Photothermal Spectroscopy Using Suspended Silicon-on-Insulator Microring Resonators. *ACS Sens.* **2016**, *1* (11), 1301-1307, DOI: 10.1021/acssensors.6b00428.
- (13) Wiesent, B.; Dorigo, D.; Koch, A. In *Limits of IR-spectrometers based on linear variable filters and detector arrays*, Instrumentation, Metrology, and Standards for Nanomanufacturing IV, San Diego, California, United States, Aug 24, 2010; SPIE: 2010; p 77670L, DOI: 10.1117/12.860532.
- (14) Wiesent, B.; Dorigo, D.; Şimşek, Ö.; Koch, A. In *Linear variable filter based oil condition monitoring systems for offshore wind turbines*, Instrumentation, Metrology, and Standards for Nanomanufacturing, Optics, and Semiconductors V, San Diego, California, United States, Sep 20, 2011; SPIE: 2011; p 81050D, DOI: 10.1117/12.891505.

- (15) Emadi, A.; Wu, H.; de Graaf, G.; Wolffenbuttel, R. F. IR Microspectrometers based on Linear-Variable Optical Filters. *Procedia Eng.* **2011**, *25*, 1401-1404, DOI: 10.1016/j.proeng.2011.12.346.
- (16) Thienpont, H.; Mohr, J.; Zappe, H.; Nakajima, H.; Ayerden, N. P.; Ghaderi, M.; Silva, M. F.; Emadi, A.; Enoksson, P.; Correia, J. H.; de Graaf, G.; Wolffenbuttel, R. F. In *Design, fabrication and characterization of LVOF-based IR microspectrometers*, Micro-Optics 2014, Brussels, Belgium, May 2, 2014; SPIE: 2014; p 91300T, DOI: 10.1117/12.2052620.
- (17) Ghaderi, M.; Ayerden, N. P.; Emadi, A.; Enoksson, P.; Correia, J. H.; de Graaf, G.; Wolffenbuttel, R. F. Design, fabrication and characterization of infrared LVOFs for measuring gas composition. *J. Micromech. Microeng.* **2014**, *24* (8), DOI: 10.1088/0960-1317/24/8/084001.
- (18) Wang, A.; Dan, Y. Mid-infrared plasmonic multispectral filters. *Sci. Rep.* **2018**, *8* (1), 1-7.
- (19) Craig, B.; Shrestha, V. R.; Meng, J.; Cadusch, J. J.; Crozier, K. B. Experimental demonstration of infrared spectral reconstruction using plasmonic metasurfaces. *Opt. Lett.* **2018**, *43* (18), 4481-4484, DOI: 10.1364/OL.43.004481.
- (20) Craig, B. J.; Meng, J.; Shrestha, V. R.; Cadusch, J. J.; Crozier, K. B. Mid- to long-wave infrared computational spectroscopy using a subwavelength coaxial aperture array. *Sci. Rep.* **2019**, *9* (1), 13537, DOI: 10.1038/s41598-019-49593-0.
- (21) Druy, M. A.; Emadi, A.; Brown, C. D.; Wu, H.; de Graaf, G.; Crocombe, R. A.; Wolffenbuttel, R. F., CMOS-compatible LVOF-based visible microspectrometer. In *Next-Generation Spectroscopic Technologies III*, 2010; p 76800W.
- (22) Bao, J.; Bawendi, M. G. A colloidal quantum dot spectrometer. *Nature* **2015**, *523* (7558), 67-70, DOI: 10.1038/nature14576.
- (23) Huang, E.; Ma, Q.; Liu, Z. Etalon array reconstructive spectrometry. *Sci. Rep.* **2017**, *7*, 40693.
- (24) Wang, Z.; Yi, S.; Chen, A.; Zhou, M.; Luk, T. S.; James, A.; Nogan, J.; Ross, W.; Joe, G.; Shahsafi, A.; Wang, K. X.; Kats, M. A.; Yu, Z. Single-shot on-chip spectral sensors based on photonic crystal slabs. *Nat. Commun.* **2019**, *10* (1), 1020, DOI: 10.1038/s41467-019-08994-5.
- (25) Brolo, A. G.; Gordon, R.; Leathem, B.; Kavanagh, K. L. Surface plasmon sensor based on the enhanced light transmission through arrays of nanoholes in gold films. *Langmuir* **2004**, *20* (12), 4813-4815, DOI: 10.1021/la0493621.
- (26) Šikola, T.; Kekatpure, R. D.; Barnard, E. S.; White, J. S.; Van Dorpe, P.; Břinec, L.; Tomanec, O.; Zlámal, J.; Lei, D. Y.; Sonnefraud, Y.; Maier, S. A.; Humlíček, J.; Brongersma, M. L. Mid-IR plasmonic antennas on silicon-rich oxinitride absorbing substrates: Nonlinear scaling of resonance wavelengths with antenna length. *Appl. Phys. Lett.* **2009**, *95* (25), DOI: 10.1063/1.3278593.
- (27) Chen, Q.; Cumming, D. R. High transmission and low color cross-talk plasmonic color filters using triangular-lattice hole arrays in aluminum films. *Opt. Express* **2010**, *18* (13), 14056-62, DOI: 10.1364/OE.18.014056.
- (28) Zhong, Y.; Malagari, S. D.; Hamilton, T.; Wasserman, D. M. Review of mid-infrared plasmonic materials. *J. Nanophotonics* **2015**, *9* (1), 093791, DOI: 10.1117/1.JNP.9.093791.
- (29) Chen, Y.; Kotnala, A.; Yu, L.; Zhang, J.; Gordon, R. Wedge and gap plasmonic resonances in double nanoholes. *Opt. Express* **2015**, *23* (23), 30227-36, DOI: 10.1364/OE.23.030227.
- (30) Chong, X.; Li, E.; Squire, K.; Wang, A. X. On-chip near-infrared spectroscopy of CO₂ using high resolution plasmonic filter array. *Appl. Phys. Lett.* **2016**, *108* (22), 221106, DOI: 10.1063/1.4953261.
- (31) Braun, A.; Maier, S. A. Versatile Direct Laser Writing Lithography Technique for Surface Enhanced Infrared Spectroscopy Sensors. *ACS Sens.* **2016**, *1* (9), 1155-1162, DOI: 10.1021/acssensors.6b00469.
- (32) Shah, Y. D.; Grant, J.; Hao, D.; Kenney, M.; Pusino, V.; Cumming, D. R. S. Ultra-narrow Line Width Polarization-Insensitive Filter Using a Symmetry-Breaking Selective Plasmonic Metasurface. *ACS Photonics* **2017**, *5* (2), 663-669, DOI: 10.1021/acsp Photonics.7b01011.
- (33) He, X.; Liu, Y.; Ganesan, K.; Ahnood, A.; Beckett, P.; Eftekhari, F.; Smith, D.; Uddin, M. H.; Skafidas, E.; Nirmalathas, A.; Unnithan, R. R. A single sensor based multispectral imaging camera using a narrow spectral band color mosaic integrated on the monochrome CMOS image sensor. *APL Photonics* **2020**, *5* (4), DOI: 10.1063/1.5140215.

- (34) Zhou, J.; Huang, B.; Yan, Z.; Bunzli, J. G. Emerging role of machine learning in light-matter interaction. *Light: Sci. Appl.* **2019**, *8*, 84, DOI: 10.1038/s41377-019-0192-4.
- (35) Ouyang, W.; Aristov, A.; Lelek, M.; Hao, X.; Zimmer, C. Deep learning massively accelerates super-resolution localization microscopy. *Nat. Biotechnol.* **2018**, *36* (5), 460-468, DOI: 10.1038/nbt.4106.
- (36) Nehme, E.; Weiss, L. E.; Michaeli, T.; Shechtman, Y. Deep-STORM: super-resolution single-molecule microscopy by deep learning. *Optica* **2018**, *5* (4), 458-464, DOI: 10.1364/OPTICA.5.000458.
- (37) Ma, W.; Cheng, F.; Liu, Y. Deep-learning-enabled on-demand design of chiral metamaterials. *ACS Nano* **2018**, *12* (6), 6326-6334, DOI: 10.1021/acsnano.8b03569.
- (38) Malkiel, I.; Mrejen, M.; Nagler, A.; Arieli, U.; Wolf, L.; Suchowski, H. Plasmonic nanostructure design and characterization via deep learning. *Light: Sci. Appl.* **2018**, *7* (1), 1-8, DOI: 10.1038/s41377-018-0060-7.
- (39) Gao, L.; Li, X.; Liu, D.; Wang, L.; Yu, Z. A Bidirectional Deep Neural Network for Accurate Silicon Color Design. *Adv. Mater.* **2019**, *31* (51), e1905467, DOI: 10.1002/adma.201905467.
- (40) Li, L.; Ruan, H.; Liu, C.; Li, Y.; Shuang, Y.; Alù, A.; Qiu, C.-W.; Cui, T. J. Machine-learning reprogrammable metasurface imager. *Nat. Commun.* **2019**, *10* (1), 1-8, DOI: 10.1038/s41467-019-09103-2.
- (41) Li, L.; Shuang, Y.; Ma, Q.; Li, H.; Zhao, H.; Wei, M.; Liu, C.; Hao, C.; Qiu, C.-W.; Cui, T. J. Intelligent metasurface imager and recognizer. *Light: Sci. Appl.* **2019**, *8* (1), 1-9, DOI: 10.1038/s41377-019-0209-z.
- (42) Schroeder, V.; Evans, E. D.; Wu, Y. M.; Voll, C. A.; McDonald, B. R.; Savagatrup, S.; Swager, T. M. Chemiresistive Sensor Array and Machine Learning Classification of Food. *ACS Sens.* **2019**, *4* (8), 2101-2108, DOI: 10.1021/acssensors.9b00825.
- (43) Hayasaka, T.; Lin, A.; Copa, V. C.; Lopez, L. P.; Loberternos, R. A.; Ballesteros, L. I. M.; Kubota, Y.; Liu, Y.; Salvador, A. A.; Lin, L. An electronic nose using a single graphene FET and machine learning for water, methanol, and ethanol. *Microsyst. Nanoeng.* **2020**, *6* (1), 1-13, DOI: 10.1038/s41378-020-0161-3.
- (44) Shrestha, V. R.; Craig, B.; Meng, J.; Bullock, J.; Javey, A.; Crozier, K. B. Mid- to long-wave infrared computational spectroscopy with a graphene metasurface modulator. *Sci. Rep.* **2020**, *10* (1), 5377, DOI: 10.1038/s41598-020-61998-w.
- (45) Xie, L.; Gao, W.; Shu, J.; Ying, Y.; Kono, J. Extraordinary sensitivity enhancement by metasurfaces in terahertz detection of antibiotics. *Sci. Rep.* **2015**, *5* (1), 1-4, DOI: 10.1038/srep08671.
- (46) Romano, S.; Zito, G.; Torino, S.; Calafiore, G.; Penzo, E.; Coppola, G.; Cabrini, S.; Rendina, I.; Mocella, V. Label-free sensing of ultralow-weight molecules with all-dielectric metasurfaces supporting bound states in the continuum. *Photonics Res.* **2018**, *6* (7), 726-733, DOI: 10.1364/PRJ.6.000726.
- (47) Tittl, A.; Leitis, A.; Liu, M.; Yesilkoy, F.; Choi, D.-Y.; Neshev, D. N.; Kivshar, Y. S.; Altug, H. Imaging-based molecular barcoding with pixelated dielectric metasurfaces. *Science* **2018**, *360* (6393), 1105-1109, DOI: 10.1126/science.aas9768.
- (48) Leitis, A.; Tittl, A.; Liu, M.; Lee, B. H.; Gu, M. B.; Kivshar, Y. S.; Altug, H. Angle-multiplexed all-dielectric metasurfaces for broadband molecular fingerprint retrieval. *Sci. Adv.* **2019**, *5* (5), eaaw2871, DOI: 10.1126/sciadv.aaw2871.
- (49) Yesilkoy, F.; Arvelo, E. R.; Jahani, Y.; Liu, M.; Tittl, A.; Cevher, V.; Kivshar, Y.; Altug, H. Ultrasensitive hyperspectral imaging and biodetection enabled by dielectric metasurfaces. *Nat. Photonics* **2019**, *13* (6), 390-396, DOI: 10.1038/s41566-019-0394-6.
- (50) Edwards, D. F. Silicon (Si). In *Handbook of optical constants of solids*; Palik, E. D., Ed.; Academic press: London, 1985; pp 547-569, DOI: 10.1016/C2009-0-20920-2.
- (51) Shiles, E.; Sasaki, T.; Inokuti, M.; Smith, D. Y. Self-consistency and sum-rule tests in the Kramers-Kronig analysis of optical data: Applications to aluminum. *Phys. Rev. B* **1980**, *22* (4), 1612-1628, DOI: 10.1103/PhysRevB.22.1612.

- (52) Sharpe, S. W.; Johnson, T. J.; Sams, R. L.; Chu, P. M.; Rhoderick, G. C.; Johnson, P. A. Gas-phase databases for quantitative infrared spectroscopy. *Appl. Spectrosc.* **2004**, *58* (12), 1452-1461, DOI: 10.1366/0003702042641281.
- (53) Harrison, J. J.; Humpage, N.; Allen, N. D.; Waterfall, A. M.; Bernath, P. F.; Remedios, J. J. Mid-infrared absorption cross sections for acetone (propanone). *J. Quant. Spectrosc. Radiat. Transfer* **2011**, *112* (3), 457-464, DOI: 10.1016/j.jqsrt.2010.09.002.
- (54) Kochanov, R. V.; Gordon, I.; Rothman, L.; Wcisło, P.; Hill, C.; Wilzewski, J. HITRAN Application Programming Interface (HAPI): A comprehensive approach to working with spectroscopic data. *J. Quant. Spectrosc. Radiat. Transfer* **2016**, *177*, 15-30, DOI: 10.1016/j.jqsrt.2016.03.005.
- (55) Kochanov, R. V.; Gordon, I. E.; Rothman, L. S.; Shine, K.; Sharpe, S.; Johnson, T.; Wallington, T.; Harrison, J.; Bernath, P.; Birk, M. Infrared absorption cross-sections in HITRAN2016 and beyond: Expansion for climate, environment, and atmospheric applications. *J. Quant. Spectrosc. Radiat. Transfer* **2019**, *230*, 172-221, DOI: 10.1016/j.jqsrt.2019.04.001.
- (56) FLIR, FLIR LEPTON Engineering Datasheet. 2019.
- (57) Altman, N. S. An introduction to kernel and nearest-neighbor nonparametric regression. *Amer. Statist.* **1992**, *46* (3), 175-185, DOI: doi.org/10.2307/2685209.
- (58) Utgoff, P. E. Incremental induction of decision trees. *Mach. Learn.* **1989**, *4* (2), 161-186, DOI: 10.1023/A:1022699900025.
- (59) Fisher, R. A. The use of multiple measurements in taxonomic problems. *Ann. Eugen.* **1936**, *7* (2), 179-188.
- (60) Dreiseitl, S.; Ohno-Machado, L. Logistic regression and artificial neural network classification models: a methodology review. *J. Biomed. Inf.* **2002**, *35* (5-6), 352-359, DOI: 10.1016/S1532-0464(03)00034-0.
- (61) Cortes, C.; Vapnik, V. Support-vector networks. *Mach. Learn.* **1995**, *20* (3), 273-297, DOI: 10.1007/BF00994018.
- (62) Fürnkranz, J. Round robin classification. *J. Mach. Learn. Res.* **2002**, *2* (Mar), 721-747, DOI: 10.1162/153244302320884605.
- (63) Escalera, S.; Pujol, O.; Radeva, P. Separability of ternary codes for sparse designs of error-correcting output codes. *Pattern Recognit. Lett.* **2009**, *30* (3), 285-297, DOI: 10.1016/j.patrec.2008.10.002.
- (64) Alpaydin, E. Principal Component Analysis. In *Introduction to machine learning*; MIT press: Cambridge, MA, 2020; Chapter 6, pp 122-129.
- (65) Seni, G.; Elder, J. F. *Ensemble methods in data mining: improving accuracy through combining predictions*, Morgan & Claypool: 2010; Vol. 2, DOI: 10.2200/S00240ED1V01Y200912DMK002.

For Table of Contents Use Only



Title: Plasmonic mid-infrared filter array-detector array chemical classifier based on machine learning

Authors: Jiajun Meng, Jasper J. Cadusch, and Kenneth B. Crozier

TOC graphic synopsis:

Left: Schematic illustration of plasmonic filter array-detector array chemical classifier simulated in this work. Right: Visualization of chemical classification results